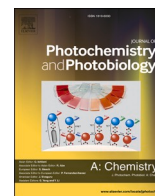




Contents lists available at ScienceDirect

Journal of Photochemistry & Photobiology, A: Chemistry

journal homepage: www.elsevier.com/locate/jphotochem

X-ray structurally characterized quinoline based fluorescent probes for pH sensing: Application in intracellular pH imaging; DFT calculations and fluorescent labelling

Subhajit Guria^a, Avijit Ghosh^{a,b}, Tanushree Mishra^a, Manas kumar Das^a, Arghya Adhikary^b, Susanta Adhikari^{a,*}

^a Department of Chemistry, University of Calcutta, 92, A.P.C. Road, Kolkata 700 009, West Bengal, India

^b Centre for Research in Nanoscience & Nanotechnology, (CRNN), University of Calcutta, Technology Campus, Sector-III, Block-JD 2, Salt Lake, Kolkata 700098, West Bengal, India

ARTICLE INFO

Keywords:

Quinoline
Fluorescent probe
DFT calculation
Intracellular pH imaging
Fluorescent labeling

ABSTRACT

Quinoline based fluorescent probes QNOH-MO and QNOH-OME were synthesized, and their photo-physical properties were carefully investigated. The probes were well characterized by ¹H-NMR, ¹³C-NMR, ESI-MS, and single-crystal X-ray structure analysis. QNOH-MO and QNOH-OME can identify small changes in pH by colorimetric and fluorescence methods. In low pH range, these probes display a red fluorescence in both live and fixed cells. However, with increasing pH, the observed red fluorescence decreased with a simultaneous increase in green fluorescence. The pH-dependent switching from red to green fluorescence is well supported by theoretical calculations and ¹H NMR titration experiments. Furthermore, the ability of these probes to image pH changes in live cells was also scrutinized. Moreover, QNOH-OME was successfully utilized for fluorescent labelling of cholesterol molecule which is an important component of biological membranes and is used in the liposomal formulation for drug delivery applications. Additionally, QNOH-MO was quaternized to induce an intrinsic cationic property to the molecule. The cationic probe QNOH-MO-CA exhibited improved water solubility and pH sensing efficiency.

1. Introduction

Acid-base (pH) balance plays a pivotal role in a myriad of cellular events, like cell growth [1] and apoptosis [2], endocytosis [3,4], signal transduction [5,6], ion transport and homeostasis [7,8]. Cells have established highly controlled mechanisms to regulate the pH of the intracellular medium and maintain normal cellular functions [9]. The tumor microenvironment is generally considered for its hypoxic nature which upsets the metabolism of the cancer cells and consequently affects the pH of the microenvironment. Cancer cell also has a higher intracellular (pH \geq 7.4) and lower extracellular pH (\sim 6.7–7.1) compared to a normal cell. This reverse pH gradient promotes cell proliferation, cancer cell invasion, and prevents apoptosis [10,11]. It also affects the uptake and efficacy of pH-sensitive chemotherapeutic drugs favouring the preferential accumulation of drugs that are weak acids [12–14]. Abnormal pH values can also result in cardiopulmonary and neurologic problems [8,9]. Within a cell, subcellular compartments such as

lysosomes, mitochondria, and endosomal vesicles, maintain pH that is different from the cytoplasmic pH (\sim 7.0) and this pH gradient have important functional consequences for these organelles [15,16]. Thus monitoring the pH in live cells is a basic need for a better understanding of physiological and pathological processes [17].

A reliable, well-established tool to measure the pH of the solution is to use an electrochemical pH sensor [18]. However; there are many disadvantages with these types of sensors including the need for frequent calibration, susceptibility to electrical interference, and corrosion in the presence of alkaline solution. They are also limited by their use in a biological environment.

To overcome these obstacles, several optical pH sensors have been developed using commercially available fluorophores that exhibit spectroscopic changes triggered by the reversible transformation in the structure of the indicator induced by pH variation. This allows acidity of the solution to be monitored using a spectrophotometer, or to visualize the pH gradient of the cellular microenvironment in real-time using a

* Corresponding author.

E-mail address: adhikarisusanta@yahoo.com (S. Adhikari).

<https://doi.org/10.1016/j.jphotochem.2020.113074>

Received 10 October 2020; Received in revised form 13 November 2020; Accepted 22 November 2020

Available online 3 December 2020

1010-6030/© 2020 Elsevier B.V. All rights reserved.

fluorescence microscope [19–24]. However, only limited probes are available that can image the event of pH changes in a ratiometric approach within live cells [25–28]. Sometimes the pH sensitive probes are also synthesized using tedious synthetic protocols [29,30]. Hence, there is adequate requirement to develop cost friendly and easy to synthesize probes that can effectively measure pH changes in real system. Herein, we have designed three pH-responsive quinoline derivatives (Fig. 1a) by employing the ICT process to bring about a ratiometric colour change for distinguishing the acidic and alkaline environment. The ability of the Intramolecular Charge Transfer (ICT) probes to produce a significant Stokes shift makes them suitable for ratiometric sensing of biologically important analytes [31–34] and intracellular pH [35–40]. Protonation of the quinoline nitrogen is an excellent strategy to promote an enhanced ICT process which would induce significant red-shifts in absorption spectra. Initially we have synthesized two probes QNOH-MO and QNOH-OME. Further introduction of cationic property in QNOH-MO produced QNOH-MO-CA which showed excellent water solubility and effectiveness. All these probes showed red fluorescence in low pH range and green in high pH range. The photophysical properties and sensitivity towards pH changes were carefully examined. To understand the origin of unique red colour observed during cells imaging experiments, we also carried out theoretical calculations and ^1H NMR titration. All these probes showed almost similar response and effectiveness towards pH changes. Hence, they could be used as excellent probes for measurement of pH.

All the Probes were characterized using ^1H -NMR, ^{13}C -NMR, Electrospray Ionization Mass Spectrometry (ESI-MS) (Figs. S1-S18, ESI), and X-ray single-crystal structure analysis (for QNOH-MO and QNOH-OME). Moreover, QNOH-OME was also successfully utilized for fluorescent labelling of cholesterol molecule which is an important component of

biological membranes and liposomal formulation.

2. Experimental

2.1. Materials and Methods

Chemicals and solvents were purchased from commercial suppliers and are used as received. ^1H and ^{13}C NMR spectra were recorded on a Bruker Avance III (300 MHz, 400 MHz, and 500 MHz) spectrometer. Chemical shifts were reported in parts per million (ppm). Multiplicity was indicated as follows: s (singlet), d (doublet), t (triplet), q (quartet), m (multiplet), dd (doublet of doublet), bs (broad singlet). Coupling constants were reported in Hertz (Hz). High resolution mass spectra were obtained on a XeVO-G2S QToF Waters spectrometer. For thin layer chromatography (TLC), Merck pre-coated TLC plates (Merck 60 F254) were used, and compounds were visualized with a UV light at 254 nm. Further visualization was achieved by staining with iodine. Flash chromatography separations were performed on SRL 230–400 mesh silica gel. Milli-Q Milipore 18.2 M Ω cm $^{-1}$ water was used throughout all experiments and in preparation of buffer solutions. A Hitachi UH-5300 spectrophotometer and a Hitachi-F7100 spectrofluorometer were used for UV–Vis and fluorescence measurements. A Labman digital pH meter (LMPH-10) was used to measure the pH of the solutions.

2.2. Cell line and cell culture

Human cervical cancer HeLa was procured from NCCS, Pune and was well maintained in heat inactivated FBS (fetal bovine serum, 10 %) containing Dulbecco's Modified Eagle's Medium (DMEM) added with 100 mg/mL concentration of antibiotics viz. penicillin, streptomycin,

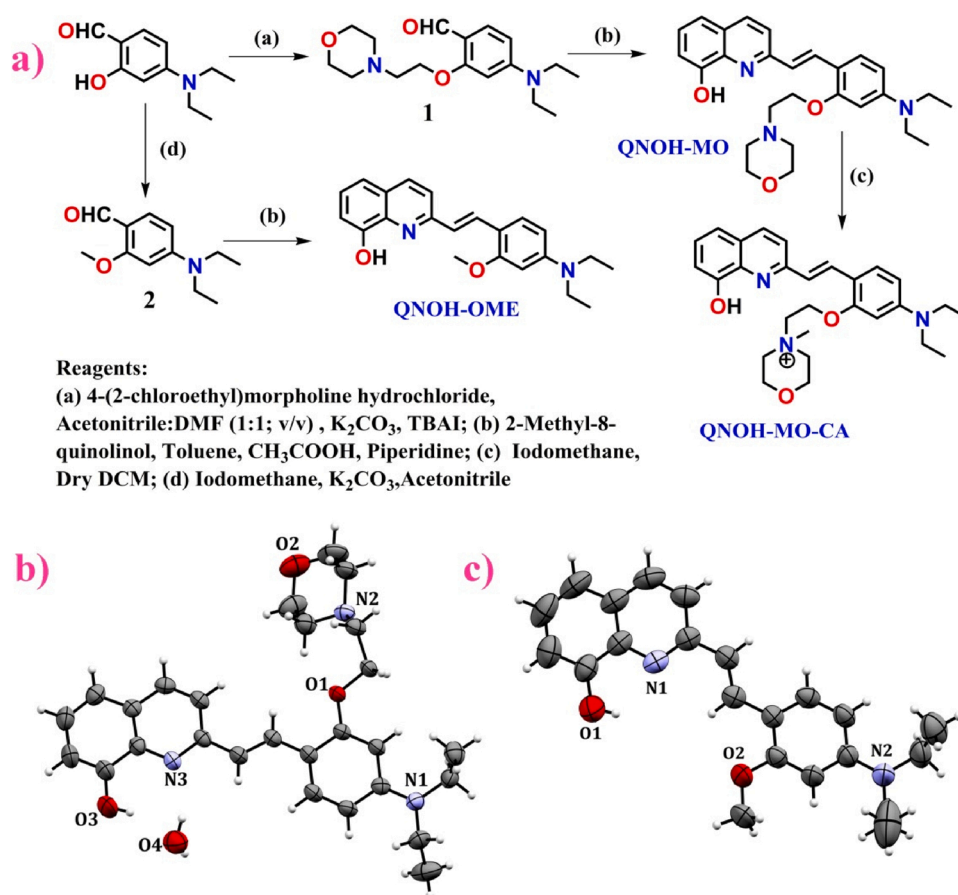


Fig. 1. (a) Synthetic route to pH sensitive quinoline derivatives QNOH-MO, QNOH-MO-CA and QNOH-OME; Single-crystal X-ray structure of (b) QNOH-MO (CCDC 2024825) and (c) QNOH-OME (CCDC 2024824).

gentamycin and amphotericin B (fungizone). Cells were incubated in a chamber humidified with 5% CO₂ to achieve 80 % of confluency, earlier to the experiment. For re-plating, cells were trypsinised; viable numbers of cells were counted (Trypan blue exclusion test) and allowed to grow in fresh medium for overnight.

2.2.1. *In vitro* live cell imaging of pH

In vitro imaging of pH in live cells was executed according to previous methods [41]. Human cervical cancer HeLa cells were cultured in Dulbecco's modified eagle medium (DMEM) supplemented with 10 % fetal bovine serum (FBS) and 1% penicillin/streptomycin at 37 °C and 5% CO₂. For *in vitro* imaging studies, the cells were seeded in 12-well tissue culture plates with a seeding density of 10⁵ cells per well. After reaching 60 %–70 % confluence, the previous DMEM medium was replaced with serum free DMEM medium. Then QNOH-MO-CA/QNOH-MO/ QNOH-OME (5 μM) was incubated for another 1 h to facilitate cellular uptake. After an hour of incubation, the cells were rinsed three times with potassium rich PBS at different pH values of 4.5, 5.5, 6.5, 7.5 or 8.5. The cells were incubated further with nigericin (1 μg/mL) for 5 min in respective potassium rich PBS buffer. Images of live cells were then taken by using an EVOS® FL Cell Imaging System, Life Technologies, USA.

2.2.2. *In vitro* cell imaging of pH in fixed cells

In vitro imaging of pH in fixed cells was carried out according to literature methods [42]. Human cervical cancer cells (HeLa) were cultured in Dulbecco's modified eagle medium (DMEM) supplemented with 10 % fetal bovine serum (FBS) and 1% penicillin/streptomycin at 37 °C and 5% CO₂. For *in vitro* imaging studies, the cells were seeded in 12-well tissue culture plates with a seeding density of 10⁵ cells per well. After reaching 60 %–70 % confluence, the previous DMEM medium was replaced with serum free DMEM medium. Then Dye (5 μM) was incubated for another 1 h to facilitate the dye uptake by cells. After that, the cells were rinsed three times with PBS and fixed in 4% paraformaldehyde for 30 min. The buffer solutions at a series of different pH levels were added in different wells to adjust the pH of fixed cells and to make sure that the intracellular pH was consistent with the surrounding buffer solution. Images of live cells were then taken by using an EVOS® FL Cell Imaging System, Life Technologies, USA.

2.2.3. Cytotoxicity assay

In vitro cytotoxicity was measured by using the colorimetric methyl thiazolyltetrazolium (MTT) assay against HeLa cells according to our previous report [43]. The Cells were seeded into 24-well tissue culture plate in presence of 500 μL Dulbecco's modified eagle medium (DMEM) supplemented with 10 % fetal bovine serum (FBS) and 1% penicillin/streptomycin at 37 °C temperature and 5 % CO₂ atmosphere for overnight and then incubated for 12–24 hours in presence of QNOH-MO-CA / QNOH-MO/ QNOH-OME at different concentrations (10–100 μM). Then cells were washed with PBS buffer and 500 μL supplemented DMEM medium was added. Subsequently, 50 μL of 3-(4,5-dimethylthiazol-2-yl)-2,5-diphenyltetrazolium bromide MTT (5 mg/mL) was added to each well and incubated for 4 h. Next, violet formazan was dissolved in 500 μL of sodium dodecyl sulfate solution in water/DMF mixture. The absorbance of solution was measured at 570 nm using microplate reader.

2.3. Synthesis

Detail synthetic procedures and characterization files of the compounds and intermediates could be found in supporting information section.

3. Result and discussion

3.1. Synthesis of the quinoline derivatives

Fig. 1a describes the synthesis of QNOH-MO, QNOH-MO-CA, and QNOH-OME using commercial precursor 4-(diethylamino)salicylaldehyde and 2-methyl-8-quinolinol. Substituting the chlorine atom of 4-(2-chloroethyl)morpholine hydrochloride with the oxygen atom of 4-(diethylamino)salicylaldehyde using K₂CO₃ as a base in (1:1) acetonitrile/DMF medium gave the intermediate compound 1 as an off-white solid in 64 % yield. This on further reaction with 2-methyl-8-quinolinol under aldol condensation gave QNOH-MO as red solid in 24 % yield. The compound was further recrystallized using a chloroform/diethylether solvent system. The crystal structure of QNOH-MO is shown in Fig. 1b. Quaternization of QNOH-MO by iodomethane in dry DCM at room temperature gave compound QNOH-MO-CA in 41 % yield. On the other hand, a substitution reaction between 4-(diethylamino)salicylaldehyde and iodomethane gave the intermediate compound 2 in 80 % yield. This under aldol reaction condition with 2-methyl-8-quinolinol gave QNOH-OME in 49 % yield, and the corresponding crystal structure is shown in Fig. 1c.

3.2. Crystal structure of QNOH-MO and QNOH-OME

The crystal structure of QNOH-MO (CCDC 2024825) shows the trans arrangement between the nitrogen (N3) atom of quinoline and the oxygen (O1) atom of the *N,N*-diethylamino benzene moiety (Fig. 1b). This is in sharp contrast to the QNOH-OME crystal structure (CCDC 2024824) where the nitrogen atom of quinoline (N1) and the oxygen (O2) atom are on the same side of the double bond (Fig. 1c). QNOH-MO also has a lattice water molecule which is hydrogen bonded to the N3 (distance ~2.040 Å) and O1 (distance 1.920 Å) atom of quinoline moiety and to the N2 (distance ~2.040 Å) atom of the morpholine unit of adjacent molecule. Such hydrogen bonding interaction leads to the formation of dimeric arrangement of the QNOH-MO molecules involving two lattice water molecules (Fig. 2a). This arrangement allows the molecule to attain a nearly planar structure between the quinoline and *N,N*-diethylamino benzene unit along the double bond with a planar angle of 5.07° (Fig. 2c), whereas for QNOH-OME the angle is 22.2° (Fig. 2d). The packing diagram of QNOH-OME revealed that the hydrogen atom (H6) opposite to quinoline nitrogen is bonded to the oxygen atom (O1) of the adjacent molecule to create a chain-like structure (Fig. 2b).

3.3. Effect of pH on the QNOH-MO and its derivatives

The optical response of QNOH-MO with varying pH conditions (pH 2–10) was studied by performing a standard pH titration experiment. The absorption spectrum of QNOH-MO is shown in Fig. 3a. In highly acidic conditions (pH~2) an intense absorption band was appeared in the region of ~375 nm and a slight hump at ~505 nm is observed. As the pH of the solution was up-regulated, the colour of the solution switches from an almost colourless to red, with an intense band at ~505 nm (Fig. 3a). On further increasing the pH, the red colour declines with the band at ~505 nm losing its intensity and stabilizing as a blue-shifted broad-band at ~425 nm (Fig. 3a: Inset). Simultaneously the bare eye colour of the solution changed from red to yellow. Furthermore, the reversible nature of the proton addition was studied by measuring the UV–vis spectrum of QNOH-MO by alternating treatment with acid and base (Fig. S19, ESI).

Similarly, the fluorescence emission spectrum of QNOH-MO was also recorded (Fig. 3b). In acidic pH region, the ligand is weakly emissive with an emission maximum at ~615 nm ($\lambda_{\text{ex}} = 490$ nm) due to the facile charge transfer that can occur between the protonated quinoline and the donor NEt₂ group [Fig. 3(b), Inset]. As the pH of the solution is gradually increased, the band at ~615 nm first increases and then decreased with a blue shift to ~575 nm ($\lambda_{\text{ex}} = 490$ nm). A band at ~550 nm

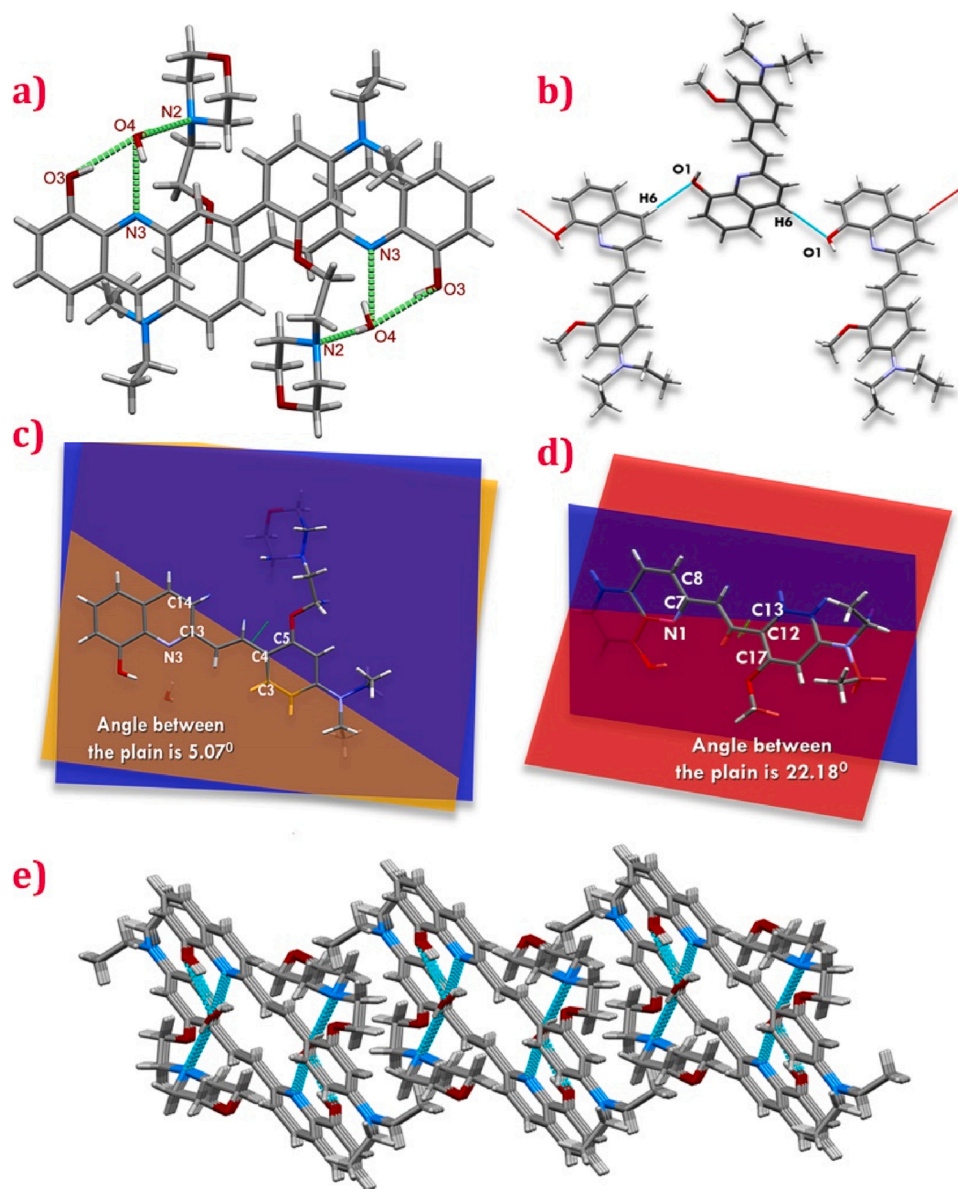


Fig. 2. (a) Hydrogen bonded dimeric arrangement of QNOH-MO; (b) packing diagram of QNOH-OME; Inter-planar angle between the quinoline moiety and the benzene ring in (c) QHOH-MO: 5.07° ; (d) QNOH-OME: 22.18° and (e) packing diagram of QNOH-MO.

($\lambda_{\text{ex}} = 380 \text{ nm}$) appears which further intensifies and moves to $\sim 530 \text{ nm}$ on increasing the pH to ~ 10 (Fig. 3b).

As two distinct colour change (i.e. from colourless to red and finally to yellow) was observed during the pH titration experiment, the working pH range was divided into two separate portions; one between pH 2.0–4.5 and the another ranging from pH 3.5–8.0 to determine the pK_a values for the probe (Fig. 3c,d). The ratio between the absorbance bands at ~ 505 and $\sim 370 \text{ nm}$ was used to calculate the pK_a in the pH range 2.0–4.5 whereas bands at ~ 505 and $\sim 430 \text{ nm}$ were taken for pH range of 3.5–8.0. The corresponding pK_a values were found to be 3.5 and 5.8 for QNOH-MO.

Additionally, a similar derivative of QNOH-MO was synthesized to systematically study the effect of the substitution present on the donor and on the acceptor moiety that is participating in the ICT process (Fig. 1a). Substituting the morpholine unit with a methoxy group produced QNOH-OME. Furthermore, quaternization of the nitrogen atom of the morpholine group in QNOH-MO by iodomethane produced QNOH-MO-CA which showed improved water solubility and in turn, is more efficient in pH sensing. UV-vis and fluorescence response of the

derivatives upon pH variation are shown in the Figs. S20-S21, ESI. To our surprise, we found that the UV-vis signature of the derivatives closely follow the response produced by QNOH-MO in the pH titration experiment. The corresponding pK_a value was found out to be 3.4 and 6.8 for QNOH-MO-CA, and 4.4 and 7.2 for QNOH-OME. Furthermore, the core unit of the donor (NEt_2) and the acceptor (quinoline-N) remain unchanged in all these derivatives. This leads us to conclude that the charge transfer process in the ground state is independent of the substitution present in the electron-donating and electron-withdrawing group.

3.4. UV-vis and fluorescence study of the quinoline derivatives

Steady-state absorption and fluorescence spectra of the quinoline derivatives were carefully examined in the presence and absence of acid in solvents of varying polarities (Figs. S22 and S23, ESI). The absorption spectrums for all the quinoline derivatives show a strong absorption band at $\sim 388\text{--}407 \text{ nm}$. However, in the case of a polar protic solvent such as ethanol, an additional red-shifted band at 525 nm was observed

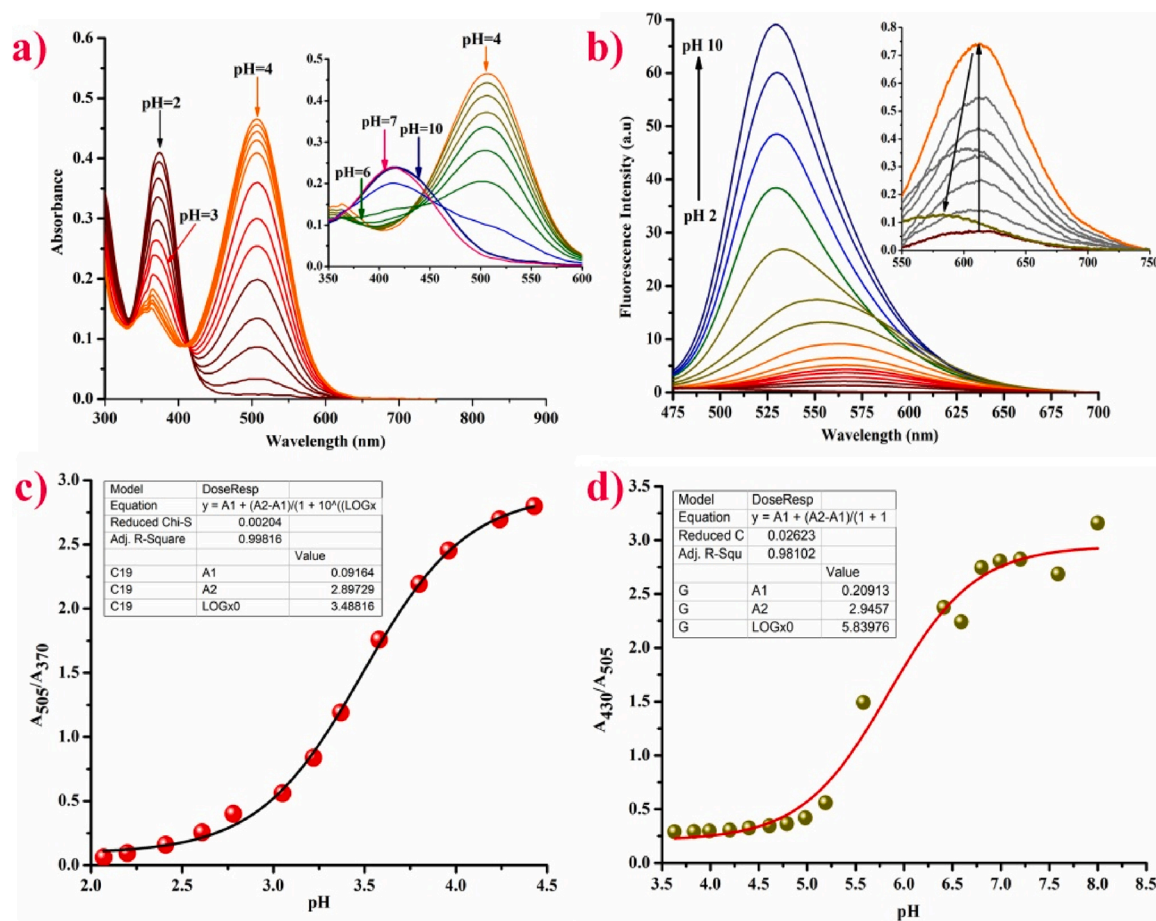


Fig. 3. (a) UV–Vis absorption spectra of QNOH-MO (20 μ M) with varying pH of the buffer solution (pH \sim 2–10) at 25 $^{\circ}$ C; (b) Fluorescence emission spectra of QNOH-MO (20 μ M) in buffer solution (pH \sim 2–10) (λ_{ex} = 380 nm) at 25 $^{\circ}$ C; (Inset: Fluorescence emission in the pH region \sim 2–5 (λ_{ex} = 490 nm)); (c) Ratio of absorbance value (A_{505} nm/ A_{370} nm) of QNOH-MO in the pH range of 2.2 to 4.5; (d) Ratio of absorbance value (A_{430} nm/ A_{505} nm) of QNOH-MO in the pH range of 3.5 to 8.0.

for all the derivatives along with the above mention bands. The addition of acid to these derivatives resulted in the formation of a new band at 527 nm with a concomitant decrease of the band at \sim 388–407 nm, in all solvents. Thus it can be assumed that the red-shifted band is due to the intramolecular charge transfer (ICT) state of the molecules induced by the protonation of quinoline nitrogen. The fluorescence spectra of these quinoline compounds in different solvents show emission maximum in the range 500–520 nm. However, in the presence of an acid, a bathochromic shift of around \sim 75–90 nm is observed in the steady-state fluorescence spectra. Hence, the systematic bathochromic shift in emission wavelength with a variation of solvent polarity suggests an ICT character of the emissive excited state of the derivatives.

The relative quantum yield of QNOH-MO was calculated in a polar protic solvent viz. ethanol in the presence ($\Phi = 0.01$, $\Phi_{ref} = 0.5$ for Rhodamine-B, $\lambda_{ex} = 500$ nm), and absence of acid ($\Phi = 0.02$, $\Phi_{ref} = 0.38$ for Coumarin-153, $\lambda_{ex} = 421$ nm). However, in chloroform the quantum yield is found to be 0.1 (10 times increase) even in presence of acid (Table S1, ESI). This indicates that a facile non-radiative decay process is operative in polar protic solvents. The TCSPC data indicates that QNOH-MO (@375 nm excitation) undergoes a non-radiative decay of the excited state in the polar protic solvents (e.g. Ethanol) due to the favourable charge transfer process initiated by the protonation of the quinoline moiety. But in polar aprotic solvents (acetonitrile: ACN; dimethylformamide: DMF) an average lifetime (τ_{avg}) of \sim 0.46 ns was observed (Table S2 ESI). The corresponding decay profile in different solvents for QNOH-MO is shown in Fig. S24a, ESI. When the solution of QNOH-MO in acetonitrile was acidified with 1eq of acid, the molecule undergoes a nonradiative decay (@450 nm excitation), and behaves

similarly to a poplar protic medium (ethanol) as indicated by the absence of fluorescence lifetime as shown in Table S2, ESI. The decay profile of QNOH-MO in presence of acid in different solvents is shown in Fig. S24b, ESI. The average lifetime and the decay profile in presence and in absence of acid for QNOH-MO-CA and QNOH-OME were summarised in Table S3-S4 and in Figs. S25 to S26, ESI.

The polarity dependent bathochromic shift in the emission maxima could be attributed to the higher dipole moment of the excited state in the quinoline derivatives. To verify this, we constructed the Lippert plot, using the Lippert equation which describes the Stokes shift ($\nu_a - \nu_f$) in terms of the changes in the dipole moment, occurring due to photoexcitation.

$$(\bar{\nu}_A - \bar{\nu}_F) = \frac{2}{hc} \left(\frac{\epsilon - 1}{2\epsilon + 1} - \frac{\eta^2 - 1}{2\eta^2 + 1} \right) \frac{(\mu_E - \mu_G)^2}{a^3} + Constant$$

The terms in the equation have their usual meaning. The quinoline derivative QNOH-MO shows a linear response with increasing values of orientation polarizability (Δf) (Fig. 4). The Onsager cavity radius necessary for the calculation of the excited state dipole moments were found to be 6.20, and 5.65 \AA for QNOH-MO, QNOH-OME using the theoretical volume calculation done on the ground state optimized geometry which is directly obtained from the density functional theory (DFT) calculations using B3LYP hybrid functional and 6–31 G(d) basis set in CPCM solvent model. The calculated values for the ground and excited-state dipole moments were found out to be 10.93 and 23.64 D for QNOH-MO, and 9.46 and 20.60 D for QNOH-OME. The corresponding Lippert – Mataga plot for QNOH-OME is shown in Fig. S27, ESI.

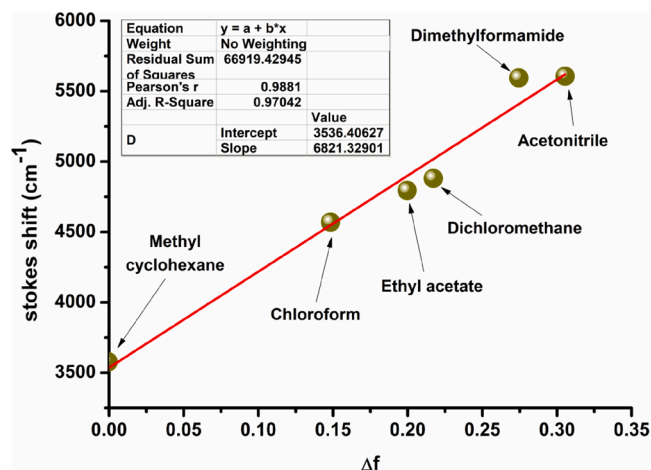


Fig. 4. Lippert–Mataga plot for QNOH-MO.

3.5. Effect of viscosity on the photo-physical property of QNOH-MO

The effect of viscosity on the absorption and the emission spectra of QNOH-MO were investigated in variable concentration of PEG-300: water medium (Fig. 5). In the absence of PEG-300, the UV–vis spectrum (Fig. 5a) of the ligand showed a peak centered at ~ 425 nm. However after reaching the concentration of PEG to approximately 20 % (V/V), a remarkable red-shifted absorption band appeared at ~ 525 nm with immediate change in the color of the solution from yellow to red. This specific band was also observed upon the addition of acid (proton source) to the solution of QNOH-MO in various solvents (Fig. S22, ESI). Thus it could be concluded that the solvation of the quinoline moiety

followed by a restricted rotation around the single bond in presence of PEG-300, facilitates the charge transfer process from the donor NEt_2 group to the solvated nitrogen of the quinoline moiety. On further increasing the concentration of PEG-300, the absorbance band at ~ 525 nm gradually decreased with a concomitant increase in the band at ~ 425 nm (Fig. 5a). Similarly, the fluorescence spectrum recorded ($\lambda_{\text{ex}} = 490$ nm) also revealed a fluorescence maxima at ~ 615 nm which corresponds to the red color observed in 20 % (V/V) of PEG-300 medium. Fluorescence intensity of this band increased upon increasing the ratios of PEG-300 followed by a hypsochromic shift to ~ 525 nm (Fig. 5c). Hence, the red emission could be attributed to the optimum viscosity of the polar protic medium.

3.6. NMR titration and probable sensing mechanism

To recognize the specific site of protonation which regulated the remarkable change in the photophysical property of QNOH-MO, a ^1H NMR titration experiment was executed using CDCl_3 as the solvent and Acetic acid- d_4 (CD_3COOD) as a proton source.

Upon addition of 1 equivalent of acid, a downfield shift from δ 2.72 to 2.83 was observed in (f) proton, indicating initial protonation to the morpholine unit. On further addition of acid protonation of the quinoline moiety occurs as indicated by the appearance of the signal (m) at δ 8.32. This results in the initiation of an intramolecular charge transfer (ICT) process as indicated by the upfield shift from δ 3.46 to 3.32 for the (c) protons of the NEt_2 group. No further changes were observed in the (f) protons indicating complete protonation of the morpholine nitrogen centre. The (g) and (h) protons were upfield shifted from δ 6.2–6.09 and from δ 6.39–6.30 indicating an increase in electron density on the benzene ring attached to the NEt_2 group. Similarly, the (k) and the (l) protons were also upfield shifted from δ 7.62 to 7.52 (Fig. 6). All the other changes in NMR δ values are given in the Table S5, ESI.

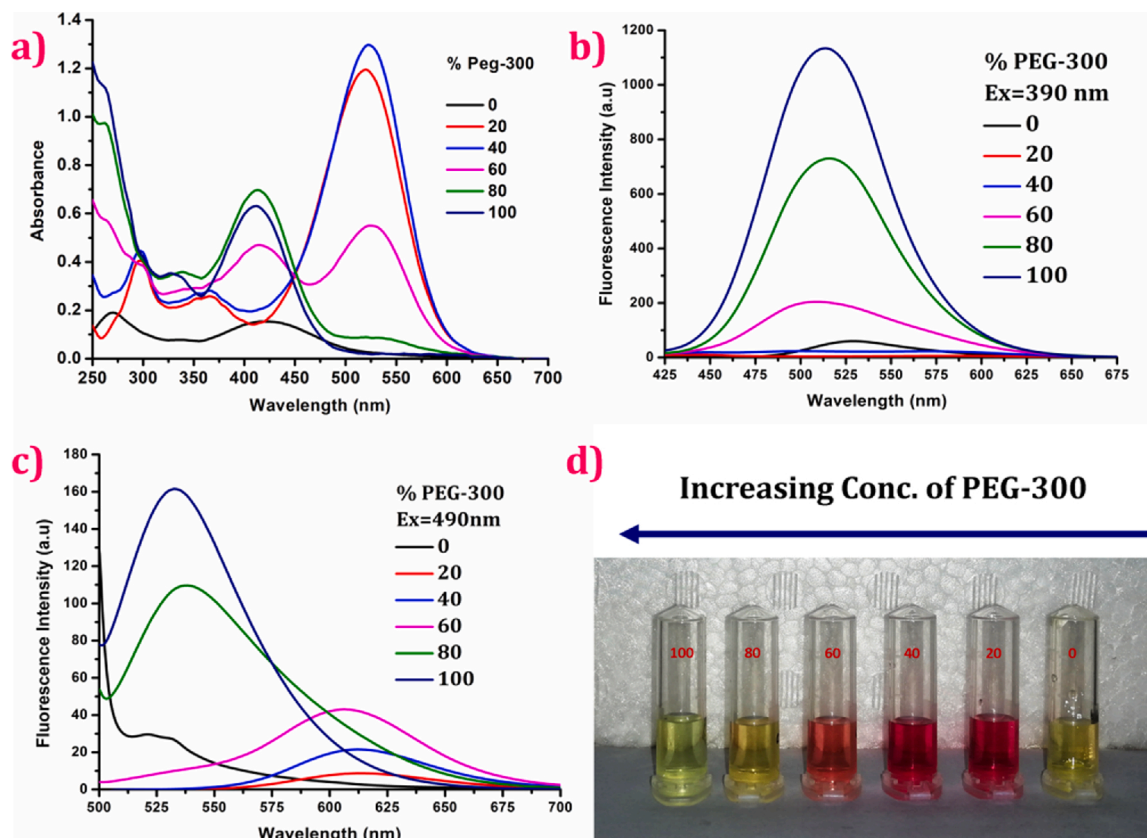


Fig. 5. Effect on absorbance (a) and fluorescence spectra of QNOH-MO (b: $\lambda_{\text{ex}} = 390$ nm) (c: $\lambda_{\text{ex}} = 490$ nm) with variation of viscosity of the medium using Peg-300/water (V/V) mixture; (d) Naked eye colour of QNOH-MO at varying concentration of PEG-300.

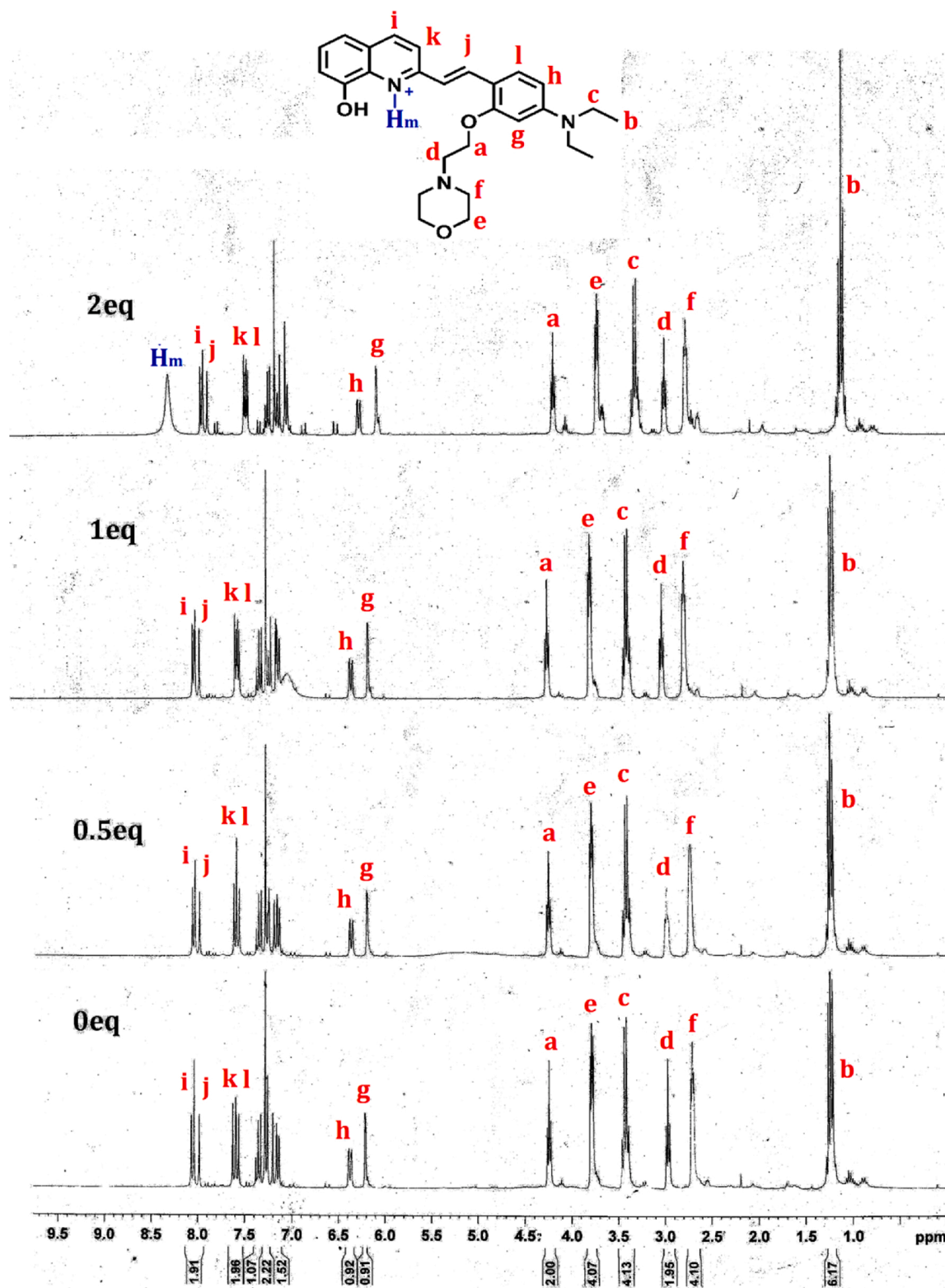


Fig. 6. ¹H NMR titration of QNOH-MO in CDCl₃; Shift of aromatic protons upon addition of increasing amount of CD₃COOD (0, 0.5, 1, 2 equivalent).

Considering all the above observations a schematic representation of the proposed mechanism is shown in Fig. 7.

3.7. Theoretical study

To understand the charge transfer process associated with the remarkable colour change of QNOH-MO in presence of an acid,

theoretical calculations were carried out using Density Functional Theory (DFT) as implemented in Gaussian 09 software [44]. Geometry optimization of QNOH-MO was carried out using Becke's three-parameter hybrid functional with LYP correlation functional (B3LYP), along with a 6–31 G(d) basis set in ethanol medium using conductor-like polarizable continuum model (C-PCM). Further, to shed light on the origin of the absorption bands of the ligand in the presence

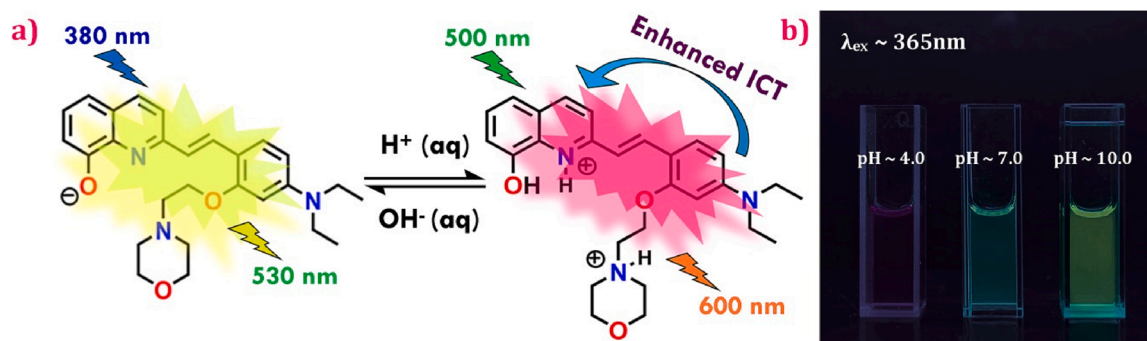


Fig. 7. (a) The proposed mechanism for colorimetric response of QNOH-MO at different pH in aqueous medium; (b) Change in fluorescence emission of QNOH-MO at different pH under UV light excitation.

and in absence of acid, TDDFT calculations were performed on the ground state optimized geometry using the above-mentioned hybrid functional and basis set. The ground state optimized structures are shown in Figs. S28 and S29. Furthermore, a comparison table describing the similarities found in solid-state and theoretical structures have been

incorporated in Table S6, ESI. A planar arrangement was observed from the dihedral angle value of $\sim 179^\circ$ between the quinoline moiety and the *N,N*-diethylamino benzyl group (C9-C17-C10-C8), indicating the presence of a facile geometry for the charge transfer process.

The corresponding dihedral angle between the *N,N*-diethylamino

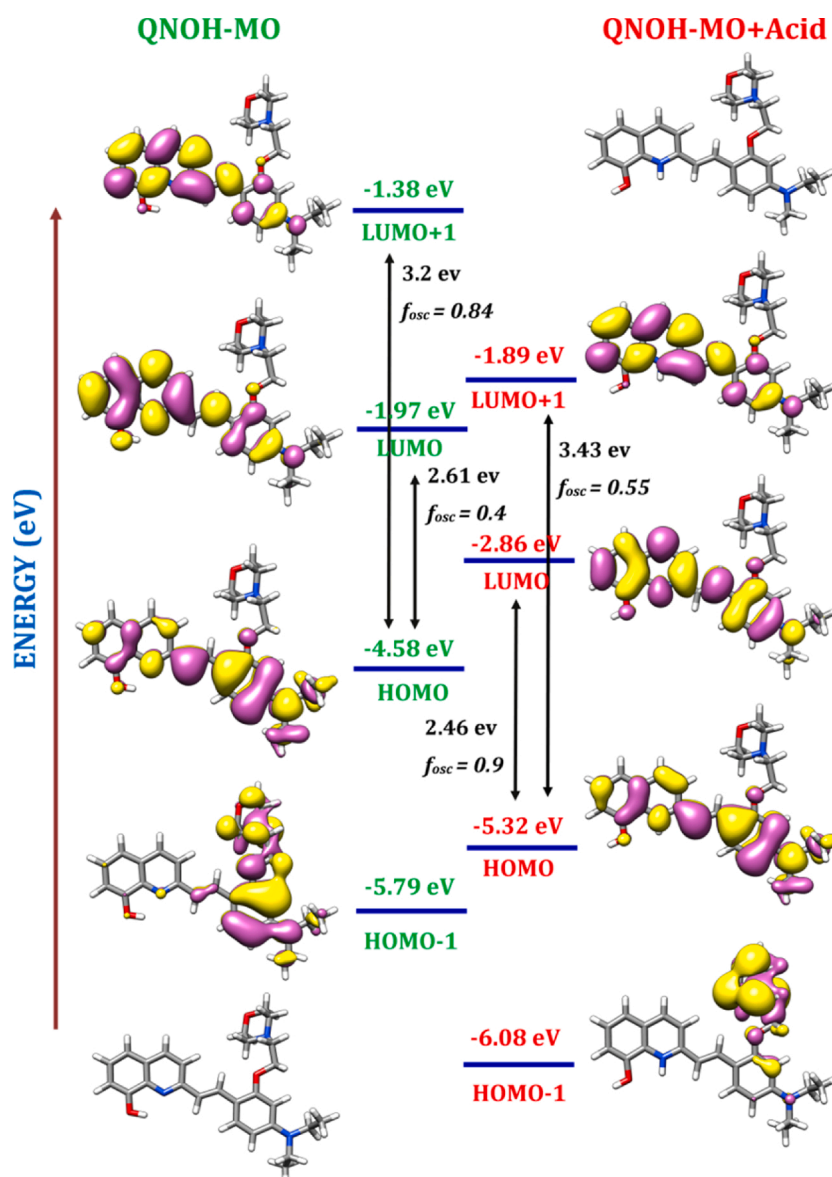


Fig. 8. HOMO-LUMO energy gap of QNOH-MO in presence and in absence of proton.

group, and the benzene group (C13-C12-N4-C34) was found to be -5.9° . The Mulliken charges for the quinoline nitrogen (N2) and *N,N*-diethylamino group nitrogen (N4) were found to be -0.678 and -0.481 . In presence of an acid, the C9-C17-C10-C8 dihedral angle remains unchanged but the C13-C12-N4-C34 dihedral angle was modified to -4.8° indicating the attainment of planarity of the electron-donating *N,N*-diethylamino group Table S6, ESI.

The equivalent molecular orbital pictures are shown in Fig. 8. It can be seen that the HOMO of QNOH-MO was present on the *N,N*-diethylamino group, and the corresponding LUMO resides on the quinoline fragment. Thus a charge transfer process can take place from HOMO to LUMO. Vertical excitation values corresponding to the first three excited states are summarized in Table S7, ESI. The percentage that a given transition contributes to the excited state is given by $2x^2$, where x represents the normalized coefficient of the transition. The first excited state of the ligand QNOH-MO comprised of two transitions, having major contribution (88 %) from (HOMO→LUMO) transition. However the oscillator strength of the transition was found to be 0.4. The corresponding theoretical wavelength was found to be ~ 516 nm which was in close agreement with the experimentally observed value of ~ 525 nm. Similarly the second excited state was also found to have been constituted by two transitions, with HOMO→LUMO+1 as the dominant one (87 %), with oscillator strength of 0.84. The corresponding theoretical and the experimental wavelength were found to be 428 and 415 nm as shown in Fig. S30, ESI. In presence of acid, the HOMO→LUMO transition of the first excited state increases in the oscillator strength to 0.9, indicating feasibility of the transition and supporting the experimental observation of the increase in the intensity of the red shifted absorbance band (Fig. S30, ESI).

4. Application

4.1. Intracellular pH imaging study

Live-cell imaging experiments were carried out to scrutinize the efficiency of these quinoline probes to image changes in the intracellular pH. The HeLa cells were cultured in Dulbecco's modified eagle medium (DMEM) supplemented with 10 % fetal bovine serum (FBS) and 1%

penicillin/streptomycin at 37°C and 5% CO_2 . Then the cells were seeded in 12-well tissue culture plates with a seeding density of 10^5 cells per well. After reaching 60 %–70 % confluence, the DMEM medium was replaced by serum free DMEM medium. Then $5\ \mu\text{M}$ of each QNOH-MO-CA was incubated for 1 h. After incubation, the cells were rinsed three times with potassium rich PBS at different pH values of 4.5, 5.5, 6.5, 7.5 or 8.5. The cells were incubated further with nigericin ($5\ \mu\text{g}/\text{mL}$) for 5 min in respective potassium rich PBS buffer. Finally, the images of live cells were then taken using a fluorescence microscope. From Fig. 9, it could be seen that at pH 4.5, fluorescence intensity in red channel was much higher compare to green channel. However, with increase in pH the emission from red channel decreases. On the other hand, the emission from green channel gradually rose at pH 5.5 and continued to increase up to pH 7.5. Hence, this cationic probe owing to its high solubility in aqueous medium could be used as an efficient marker for pH changes in live cells. It is important to mention that analogous experiments were carried out using QNOH-MO and QNOH-OME. To our delight, we found almost similar observations in both these cases. Results are summarised in Figs. S31-S32, ESI.

In the same way, the pH sensitivity of the probes at a pH lower than 4.5 was carried out by fixed cell imaging experiments. In this procedure, $5\ \mu\text{M}$ of QNOH-MO-CA was incubated for 1 h. After that, the cells were rinsed three times with PBS and fixed with 4% paraformaldehyde for 30 min. The buffer solutions of different pH levels (pH 3–7.4) were added in different wells to adjust the pH of fixed cells keeping the intracellular pH consistent with the surrounding buffer medium. Images of fixed cells were then taken by a fluorescence microscope (Fig. 10).

From the experiment, we found that the probe showed emission at red channel up to pH 4.6. The emission from the green channel was negligible in this pH range. Conversely, from pH 5, the fluorescence from green channel increases and reaches maximum at pH 7.5. In this pH ranges, no significant emission from red channel was observed. All these cumulative results suggested that these probes could be used to measure intracellular pH changes in both live and fixed cells. The other two probes QNOH-MO and QNOH-OME also showed the similar observations (Figs. S33-S34, ESI).

Nevertheless, as we discussed earlier that water solubility of the probe QNOH-MO-CA is much higher than other two probes and

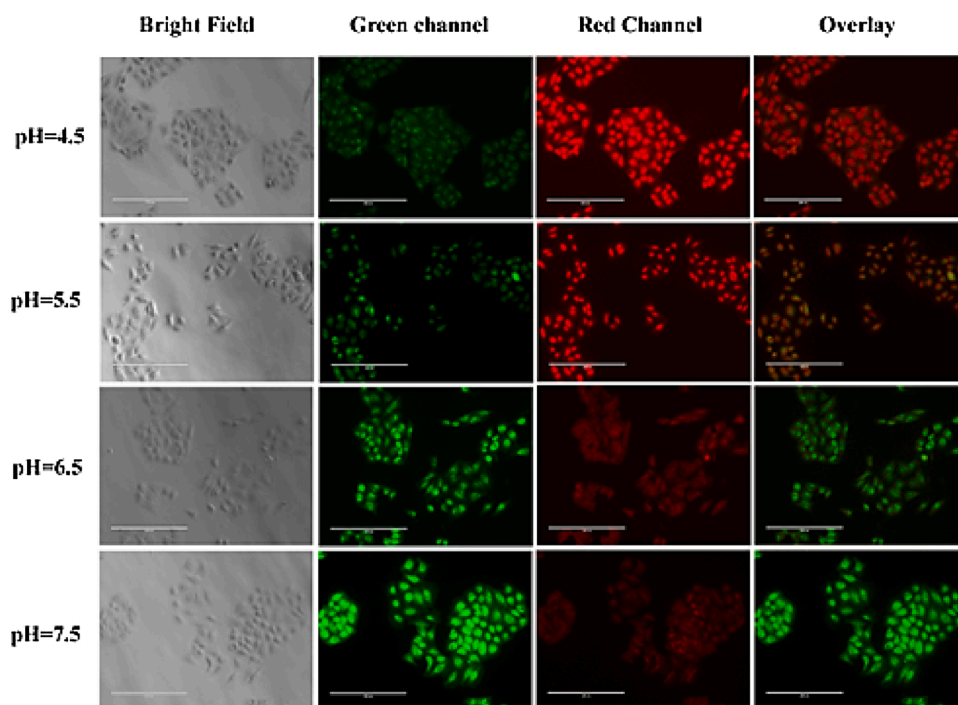


Fig. 9. Imaging of QNOH-MO-CA at different pH in live cells.

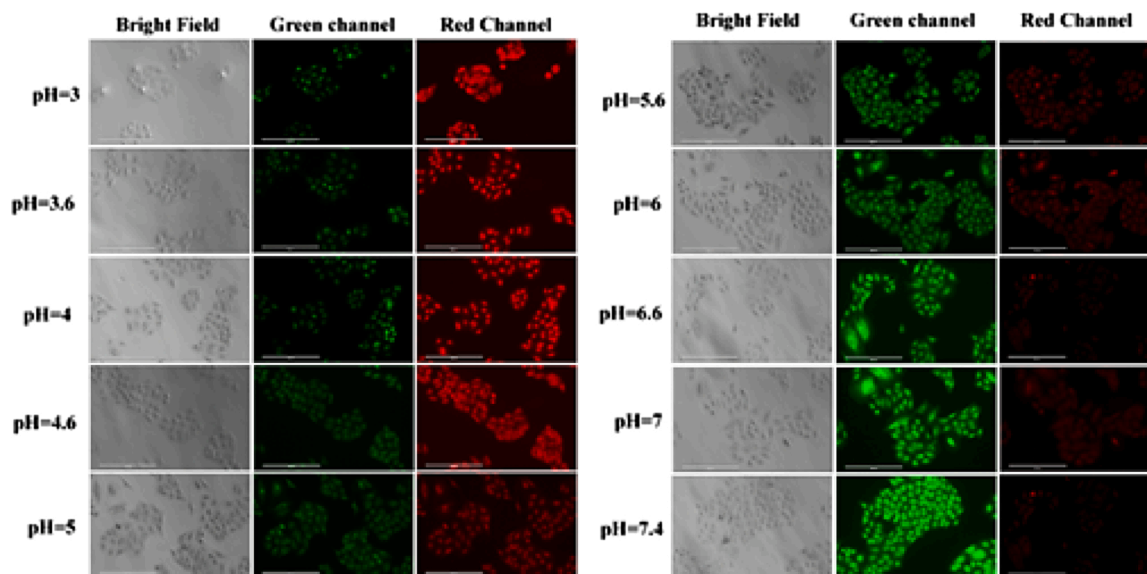


Fig. 10. Imaging of QNOH-MO-CA at different pH in fixed cells.

therefore QNOH-MO-CA is much easier to use in biological experiments. However, probes QNOH-MO and QNOH-OME are also equally effective towards measurement of pH in live or fixed cells. Furthermore, we carefully examined the localization of the probe QNOH-MO-CA in live cells with Hoechst stain (Fig. 11).

From the experiment, it was observed that the probe mainly localizes in the lysosome of cells at biological pH of 7.4. It could be assumed that the presence of a morpholine unit in the structure of QNOH-MO-CA, allows it to preferentially concentrate in the lysosome. However, it is interesting to note that at a lower pH range (3–4.5), QNOH-MO-CA specifically restricts to the nucleus of cells (Fig. S35, ESI). Hence, it could be used as a nucleus staining for fixed cells at a low pH range.

Nevertheless, the toxicity of each probe were carefully scrutinized in HeLa cells by MTT assay. From the results, it was observed that these probes are nontoxic in live cells (Figs. S36-S38, ESI). Therefore, all these quinoline derivatives could be used as an excellent probe for detection of pH changes in live cells.

4.2. Fluorescent labelling application of CHQN-OME

We further utilized the fluorescent property of QNOH-OME to label biologically significant molecules like cholesterol. Several fluorescent lipids and cholesterol derivatives were synthesised that are used in developing fluorescent liposomes to image the delivery of therapeutic agents to cancer cells, to track the dynamics of cationic lipids in the cellular environment, and to study lipid microdomains [45–48]. However, all these methods require tedious multistep synthesis and purification protocols for obtaining the fluorescent lipid/cholesterol derivatives. Hence, there is still a requirement for a cost-friendly, nontoxic fluorophore to label cholesterol. We have tagged QNOH-OME with a cholesterol molecule by a simple substitution reaction (Fig. 12). The photophysical property of the fluorescent cholesterol derivative (CHQN-OME) is studied in varying pH conditions (Figs. S39-S40 ESI). The live-cell imaging application of CHQN-OME (Fig. 12) highlights the excellent fluorescence property and good cell permeability of the ligand. Thus QNOH-OME could serve as an excellent

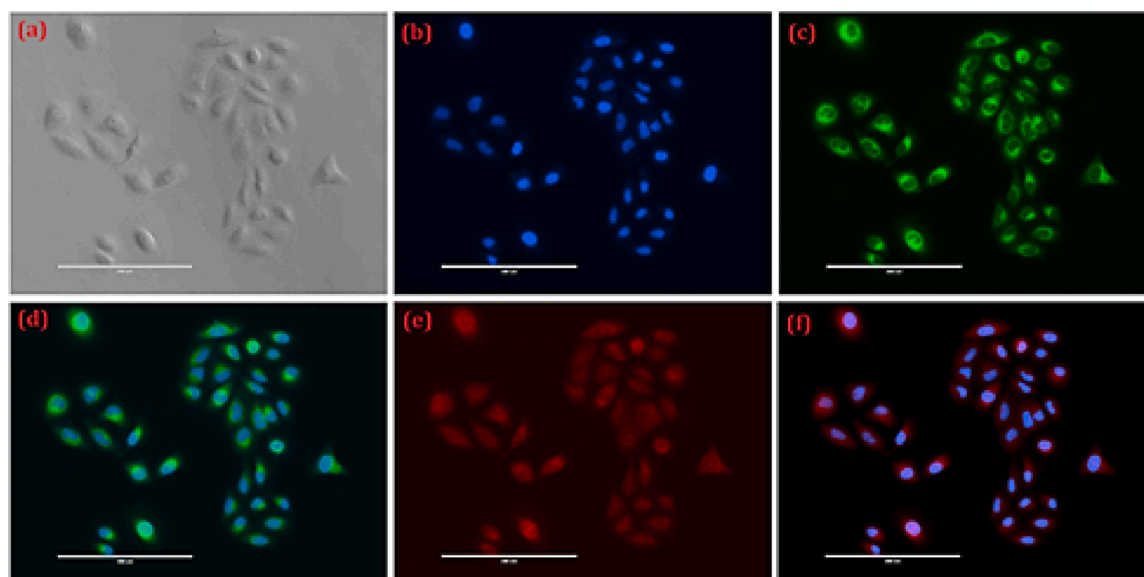


Fig. 11. Localization of QNOH-MO-CA in live cells.

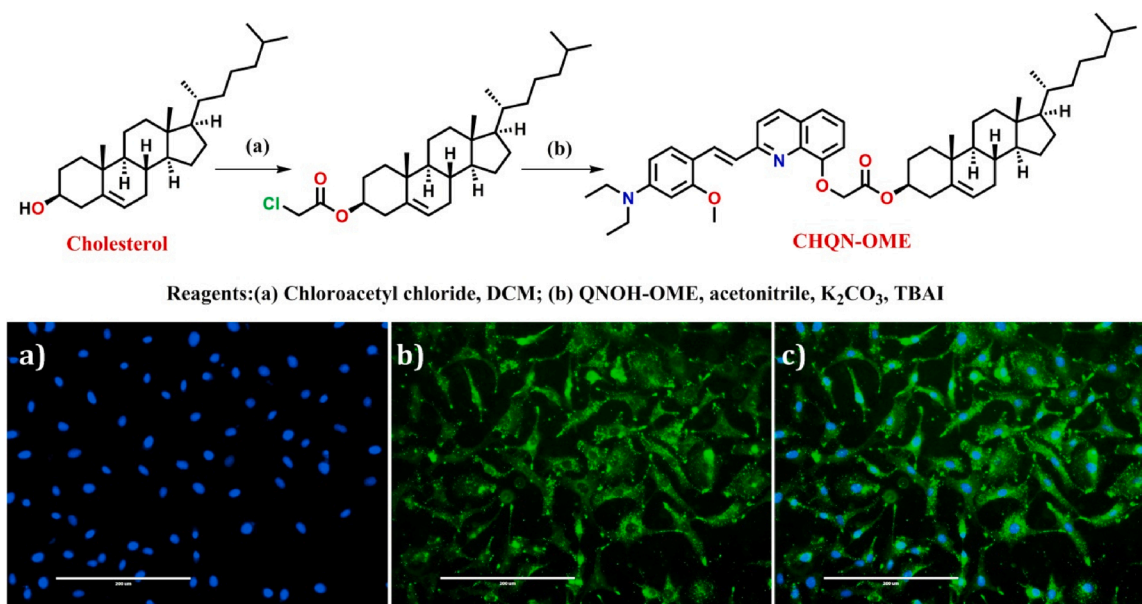


Fig. 12. (upper panel) Synthetic route to CHQN-OME; (lower panel) Fluorescence cell images of HeLa cells using CHQN-OME (a) blue channel image of cells after incubating with Hoechst and CHQN-OME (20 μ M); (b) green channel image of the cells; (c) Overlay images of (a) and (b) (scale bar 200 μ m).

marker for labelling molecules like cholesterol. Moreover, we also hope that CHQN-OME could be used in future to develop fluorescent liposomes for image-guided therapy.

5. Conclusions

Overall we have developed quinoline based fluorescent probes QNOH-MO and QNOH-OME and their photo-physical property was examined carefully. The probes were characterized by ¹H NMR, ¹³C NMR, HRMS and single crystal X-ray structure. QNOH-MO and QNOH-OME are able to identify small changes in pH by colorimetric and fluorescence methods. In low pH range, these probes displayed red fluorescence in both live and fixed cells. However, with increasing pH, the observed red fluorescence decreases with a simultaneous increase in green fluorescence. The appearance of unique red fluorescence from cellular environment may attribute from combined effect of acidic pH and viscosity or hydrophobicity. This phenomenon was resolved by theoretical calculations and ¹H NMR titration experiments. Additionally, quaternization of the morpholine unit in QNOH-MO induced an intrinsic cationic property to the molecule. The cationic probe QNOH-MO-CA showed improved water solubility as well as pH sensing efficiency. Furthermore, QNOH-OME has been utilized as an excellent marker for fluorescent labelling of cholesterol molecules which is an important component of all biological membranes as well as in liposomal formulation for drug delivery applications. Therefore, all these cumulative result suggested that the molecules could be used as cost effective and easily available probes for measurement of pH changes.

Note

The crystal structure data can be obtained free of charge via The Cambridge Crystallographic Data Centre at <https://www.ccdc.cam.ac.uk>.

CRedit authorship contribution statement

Subhajit Guria: Conceptualization, Methodology, Data curation, Writing - review & editing. **Avijit Ghosh:** Conceptualization, Methodology, Data curation, Writing - review & editing. **Tanushree Mishra:** Formal analysis, Data curation. **Manas kumar Das:** Formal analysis,

Data curation. **Arghya Adhikary:** Visualization, Formal analysis, Resources. **Susanta Adhikari:** Supervision, Project administration, Funding acquisition, Writing - review & editing.

Declaration of Competing Interest

There are no conflicts to declare.

Acknowledgements

S.G. acknowledges CSIR for financial support. S.A. is thankful to SERB-DST, New Delhi, India (project no. EMR/2017/002140), for financial assistance, and T.M. acknowledges the same for the JRF fellowship. A.G. and A.A. are grateful to DST Nanomission and M.K.D. to DSKPDF (UGC) for financial support. The authors are thankful to Ms. Somali Mukherjee for helping them with the crystal data.

Appendix A. Supplementary data

Supplementary material related to this article can be found, in the online version, at doi:<https://doi.org/10.1016/j.jphotochem.2020.113074>.

References

- [1] C.Q. Sun, C.J. O'Connor, S.J. Turner, G.D. Lewis, R.A. Stanley, A.M. Robertson, The effect of pH on the inhibition of bacterial growth by physiological concentrations of butyric acid: implications for neonates fed on suckled milk, *Chem. Biol. Interact.* 113 (1998) 117–131, [https://doi.org/10.1016/S0009-2797\(98\)00025-8](https://doi.org/10.1016/S0009-2797(98)00025-8).
- [2] D. Lagadic-Gossmann, L. Huc, V. Lecureur, Alterations of intracellular pH homeostasis in apoptosis: origins and roles, *Cell Death Differ.* 11 (2004) 953–961, <https://doi.org/10.1038/sj.cdd.4401466>.
- [3] M.J. Geisow, W.H. Evans, pH in the endosome. Measurements during pinocytosis and receptor-mediated endocytosis, *Exp. Cell Res.* 150 (1984) 36–46, [https://doi.org/10.1016/0014-4827\(84\)90699-2](https://doi.org/10.1016/0014-4827(84)90699-2).
- [4] I. Mellman, R. Fuchs, A. Helenius, Acidification of the endocytic and exocytic pathways, *Annu. Rev. Biochem.* 55 (1986) 663–700, <https://doi.org/10.1146/annurev.bi.55.070186.003311>.
- [5] R.A. Cardone, V. Casavola, S.J. Reshkin, The role of disturbed pH dynamics and the NA⁺/H⁺ exchanger in metastasis, *Nat. Rev. Cancer* 5 (2005) 786–795, <https://doi.org/10.1038/nrc1713>.
- [6] S. Negrete-Urtasun, S.H. Denison, H.N. Arst, Characterization of the pH signal transduction pathway gene *paA* of *Aspergillus nidulans* and identification of possible homologs, *J. Bacteriol.* 179 (1997) 1832–1835, <https://doi.org/10.1128/jb.179.5.1832-1835.1997>.

- [7] E. Bassil, A. Coku, E. Blumwald, Cellular ion homeostasis: emerging roles of intracellular NHX Na⁺/H⁺ antiporters in plant growth and development, *J. Exp. Bot.* 63 (2012) 5727–5740, <https://doi.org/10.1093/jxb/ers250>.
- [8] W. Aoi, Y. Marunaka, Importance of pH homeostasis in metabolic health and diseases: crucial role of membrane proton transport, *Biomed Res. Int.* 2014 (2014), <https://doi.org/10.1155/2014/598986>.
- [9] J.K. Pittman, Multiple transport pathways for mediating intracellular pH homeostasis: the contribution of H⁺/ion exchangers, *Front. Plant Sci.* 3 (2012) 11, <https://doi.org/10.3389/fpls.2012.00011>.
- [10] S.I. Wanandi, I. Yustisia, G.M.G. Neolaka, S.W.A. Jusman, Impact of extracellular alkalinization on the survival of human CD24-/CD44+ breast cancer stem cells associated with cellular metabolic shifts, *Braz. J. Med. Biol. Res.* 50 (2017) 1–11, <https://doi.org/10.1590/1414-431x20176538>.
- [11] D.M. Prescott, H.C. Charles, J.M. Poulson, R.L. Page, D.E. Thrall, Z. Vujaskovic, M. W. Dewhirst, The relationship between intracellular and extracellular pH in spontaneous canine tumors, *Clin. Cancer Res.* 6 (2000) 2501–2505.
- [12] P. Swietach, A. Hulikova, S. Patiar, R.D. Vaughan-Jones, A.L. Harris, Importance of intracellular pH in determining the uptake and efficacy of the weakly basic chemotherapeutic drug, doxorubicin, *PLoS One* 7 (2012) e35949, <https://doi.org/10.1371/journal.pone.0035949>.
- [13] N. Raghunand, X. He, R. Van Sluis, B. Mahoney, B. Baggett, C.W. Taylor, G. Paine-Murrieta, D. Roe, Z.M. Bhujwalla, R.J. Gillies, Enhancement of chemotherapy by manipulation of tumour pH, *Br. J. Cancer* 80 (1999) 1005–1011, <https://doi.org/10.1038/sj.bjc.6690455>.
- [14] H. Kobayashi, Cancer chemotherapy specific to acidic nests, *Cancers (Basel)* 9 (2017) 36, <https://doi.org/10.3390/cancers9040036>.
- [15] J.R. Casey, S. Grinstein, J. Orlowski, Sensors and regulators of intracellular pH, *Nat. Rev. Mol. Cell Biol.* 11 (2010) 50–61, <https://doi.org/10.1038/nrm2820>.
- [16] N. Demareux, pH homeostasis of cellular organelles, *News Physiol. Sci.* 17 (2002) 1–5, <https://doi.org/10.1152/physiolonline.2002.17.1.1>.
- [17] M.M. Wu, J. Llopis, S. Adams, J.M. McCaffery, M.S. Kulomaa, T.E. Machen, H.-P. H. Moore, R.Y. Tsien, Organelle pH studies using targeted avidin and fluorescein-biotin, *Chem. Biol.* 7 (2000) 197–209, [https://doi.org/10.1016/S1074-5521\(00\)00088-0](https://doi.org/10.1016/S1074-5521(00)00088-0).
- [18] M.T. Ghoneim, A. Nguyen, N. Dereje, J. Huang, G.C. Moore, P.J. Murzynowski, C. Dagdeviren, Recent progress in electrochemical pH-Sensing materials and configurations for biomedical applications, *Chem. Rev.* 119 (2019) 5248–5297, <https://doi.org/10.1021/acs.chemrev.8b00655>.
- [19] Y. Zhang, S. Xia, M. Fang, W. Mazi, Y. Zeng, T. Johnston, A. Pap, R.L. Luck, H. Liu, New near-infrared rhodamine dyes with large Stokes shifts for sensitive sensing of intracellular pH changes and fluctuations, *Chem. Commun.* 54 (2018) 7625–7628, <https://doi.org/10.1039/c8cc03520b>.
- [20] F. Miao, S. Uchinomiya, Y. Ni, Y.-T. Chang, J. Wu, Development of pH-Responsive BODIPY probes for staining late endosome in live cells, *Chempluschem* 81 (2016) 1209–1215, <https://doi.org/10.1002/cplu.201600249>.
- [21] J.W. Chen, C.M. Chen, C.C. Chang, A fluorescent pH probe for acidic organelles in living cells, *Org. Biomol. Chem.* 15 (2017) 7936–7943, <https://doi.org/10.1039/c7ob02037f>.
- [22] J. Qi, D. Liu, X. Liu, S. Guan, F. Shi, H. Chang, H. He, G. Yang, Fluorescent pH sensors for broad-range pH measurement based on a single fluorophore, *Anal. Chem.* 87 (2015) 5897–5904, <https://doi.org/10.1021/acs.analchem.5b00053>.
- [23] K.K. Yu, J.T. Hou, K. Li, Q. Yao, J. Yang, M.Y. Wu, Y.M. Xie, X.Q. Yu, A single design strategy for dual sensitive pH probe with a suitable range to map pH in living cells, *Sci. Rep.* 5 (2015) 15540, <https://doi.org/10.1038/srep15540>.
- [24] T. Hirano, Y. Noji, T. Shiraishi, M. Ishigami-Yuasa, H. Kagechika, Development of an 'OFF-ON-OFF' fluorescent pH sensor suitable for the study of intracellular pH, *Tetrahedron* 72 (2016) 4925–4930, <https://doi.org/10.1016/j.tet.2016.06.065>.
- [25] G. Li, B. Zhang, X. Song, Y. Xia, H. Yu, X. Zhang, Y. Xiao, Y. Song, Ratiometric imaging of mitochondrial pH in living cells with a colorimetric fluorescent probe based on fluorescein derivative, *Sens. Actuators B Chem.* 253 (2017) 58–68, <https://doi.org/10.1016/j.snb.2017.06.065>.
- [26] W. Shi, X. Li, H. Ma, A tunable ratiometric pH sensor based on carbon nanodots for the quantitative measurement of the intracellular pH of whole cells, *Angew. Chemie - Int. Ed.* 51 (2012) 6432–6435, <https://doi.org/10.1002/anie.201202533>.
- [27] G. Despras, A.I. Zamaleeva, L. Dardevet, C. Tisseyre, J.G. Magalhaes, C. Garner, M. De Waard, S. Amigorena, A. Feltz, J.M. Mallet, M. Collot, H-Rubies, a new family of red emitting fluorescent pH sensors for living cells, *Chem. Sci.* 6 (2015) 5928–5937, <https://doi.org/10.1039/c5sc01113b>.
- [28] Y. Chen, C. Zhu, J. Cen, Y. Bai, W. He, Z. Guo, Ratiometric detection of pH fluctuation in mitochondria with a new fluorescein/cyanine hybrid sensor, *Chem. Sci.* 6 (2015) 3187–3194, <https://doi.org/10.1039/c4sc04021j>.
- [29] M. Fang, S. Xia, J. Bi, T.P. Wigstrom, L. Valenzano, J. Wang, W. Mazi, M. Tanasova, F.T. Luo, H. Liu, A cyanine-based fluorescent cassette with aggregation-induced emission for sensitive detection of pH changes in live cells, *Chem. Commun.* 54 (2018) 1133–1136, <https://doi.org/10.1039/c7cc08986d>.
- [30] J. Zhang, M. Yang, W. Mazi, K. Adhikari, M. Fang, F. Xie, L. Valenzano, A. Tiwari, F.T. Luo, H. Liu, Unusual fluorescent responses of morpholine-functionalized fluorescent probes to pH via manipulation of BODIPY's HOMO and LUMO energy orbitals for intracellular pH detection, *ACS Sens.* 1 (2016) 158–165, <https://doi.org/10.1021/acssensors.5b00065>.
- [31] Y. Liu, H. Fan, Y. Wen, T. Jia, Q. Su, F. Li, ICT-based near infrared fluorescent switch-on probe for nitric oxide bioimaging in vivo, *Dyes Pigm.* 166 (2019) 211–216, <https://doi.org/10.1016/j.dyepig.2019.03.012>.
- [32] X. Xia, F. Zeng, P. Zhang, J. Lyu, Y. Huang, S. Wu, An ICT-based ratiometric fluorescent probe for hydrazine detection and its application in living cells and in vivo, *Sens. Actuators B Chem.* 227 (2016) 411–418, <https://doi.org/10.1016/j.snb.2015.12.046>.
- [33] X. Wang, Y. Zuo, Y. Zhang, T. Yang, W. Lin, An ICT-based fluorescent probe with bridging Si-O-Si bonds for visualizing hydrogen sulfide in lipid droplets and its application, *Anal. Methods* 12 (2020) 1064–1069, <https://doi.org/10.1039/c9ay02657f>.
- [34] Y. Wang, J. Liu, X. Ma, C. Cui, P.R. Deenik, P.K.P. Henderson, A.L. Sigler, L. Cui, Real-time imaging of senescence in tumors with DNA damage, *Sci. Rep.* 9 (2019) 1–11, <https://doi.org/10.1038/s41598-019-38511-z>.
- [35] W. Niu, L. Fan, M. Nan, Z. Li, D. Lu, M.S. Wong, S. Shuang, C. Dong, Ratiometric emission fluorescent pH probe for imaging of living cells in extreme acidity, *Anal. Chem.* 87 (2015) 2788–2793, <https://doi.org/10.1021/ac504109h>.
- [36] X. Liu, Y. Su, H. Tian, L. Yang, H. Zhang, X. Song, J.W. Foley, Ratiometric fluorescent probe for lysosomal pH measurement and imaging in living cells using single-wavelength excitation, *Anal. Chem.* 89 (2017) 7038–7045, <https://doi.org/10.1021/acs.analchem.7b00754>.
- [37] Q. Zhu, Z. Li, L. Mu, X. Zeng, C. Redshaw, G. Wei, A quinoline-based fluorometric and colorimetric dual-modal pH probe and its application in bioimaging, *Spectrochim. Acta - Part A Mol. Biomol. Spectrosc.* 188 (2018) 230–236, <https://doi.org/10.1016/j.saa.2017.06.071>.
- [38] Z. Liu, G. Li, Y. Wang, J. Li, Y. Mi, D. Zou, T. Li, Y. Wu, Quinoline-based ratiometric fluorescent probe for detection of physiological pH changes in aqueous solution and living cells, *Talanta* 192 (2019) 6–13, <https://doi.org/10.1016/j.talanta.2018.09.026>.
- [39] S. Zhu, W. Lin, L. Yuan, Development of a ratiometric fluorescent pH probe for cell imaging based on a coumarin-quinoline platform, *Dyes Pigm.* 99 (2013) 465–471, <https://doi.org/10.1016/j.dyepig.2013.05.010>.
- [40] W.J. Zhang, L. Fan, Z.B. Li, T. Ou, H.J. Zhai, J. Yang, C. Dong, S.M. Shuang, Thiazole-based ratiometric fluorescence pH probe with large Stokes shift for intracellular imaging, *Sens. Actuators B Chem.* 233 (2016) 566–573, <https://doi.org/10.1016/j.snb.2016.04.122>.
- [41] S. Zhang, T.H. Chen, H.M. Lee, J. Bi, A. Ghosh, M. Fang, Z. Qian, F. Xie, J. Ainsley, C. Christov, F.T. Luo, F. Zhao, H. Liu, Luminescent probes for sensitive detection of pH changes in live cells through two near-infrared luminescence channels, *ACS Sens.* 2 (2017) 924–931, <https://doi.org/10.1021/acssensors.7b00137>.
- [42] P. Zhang, J. Meng, Y. Li, Z. Wang, Y. Hou, pH-sensitive ratiometric fluorescent probe for evaluation of tumor treatments, *Materials (Basel)* 12 (2019) 1–10, <https://doi.org/10.3390/ma12101632>.
- [43] S. Guria, A. Ghosh, P. Upadhyay, M. Kumar Das, T. Mishra, A. Adhikari, S. Adhikari, Small-molecule probe for sensing serum albumin with consequential self-assembly as a fluorescent organic nanoparticle for bioimaging and drug-delivery applications, *ACS Appl. Bio Mater.* 3 (2020) 3099–3113, <https://doi.org/10.1021/acsbm.0c00146>.
- [44] M.J. Frisch, G.W. Trucks, H.B. Schlegel, G.E. Scuseria, M.A. Robb, J.R. Cheeseman et al. Gaussian 09, Gaussian 09, Revis. A.02. Gaussian (2009) Inc. Wallingford CT.
- [45] L.M. Solanko, A. Honigmann, H.S. Midtby, F.W. Lund, J.R. Brewer, V. Dekaris, R. Bittman, C. Eggeling, D. Wüstner, Membrane orientation and lateral diffusion of BODIPY-cholesterol as a function of probe structure, *Biophys. J.* 105 (2013) 2082–2092, <https://doi.org/10.1016/j.bpj.2013.09.031>.
- [46] L. Skorpilová, S. Rimpelová, M. Jurásek, M. Buděšínský, J. Lokajová, R. Effenberg, P. Šlepíčka, T. Ruml, E. Kmoníčková, P.B. Drašar, Z. Wimmer, BODIPY-based fluorescent liposomes with sesquiterpene lactone trilobolide, *Beilstein J. Org. Chem.* 13 (2017) 1316–1324, <https://doi.org/10.3762/bjoc.13.128>.
- [47] C. Kleusch, N. Hersch, B. Hoffmann, R. Merkel, A. Csizsár, Fluorescent lipids: functional parts of fusogenic liposomes and tools for cell membrane labeling and visualization, *Molecules* 17 (2012) 1055–1073, <https://doi.org/10.3390/molecules17011055>.
- [48] D. O'Connor, A. Byrne, T.E. Keyes, Linker length in fluorophore-cholesterol conjugates directs phase selectivity and cellular localisation in GUVs and live cells, *RSC Adv.* 9 (2019) 22805–22816, <https://doi.org/10.1039/c9ra03905h>.